# On three-dimensional dilational elastic metamaterials



2014 New J. Phys. 16 033032

(http://iopscience.iop.org/1367-2630/16/3/033032)

New Journal of Physics
The open access journal at the forefront of physics
Deutsche Physikalische Gesellschaft DPG | IOP Institute of Physics

# On three-dimensional dilational elastic metamaterials

**Tiemo Bückmann[1], Robert Schittny[1], Michael Thiel[1,2], Muamer Kadic[1], Graeme W Milton[3] and Martin Wegener[1,4]**

[1] Institute of Applied Physics, Karlsruhe Institute of Technology (KIT), D-76128 Karlsruhe, Germany
[2] Nanoscribe GmbH, Hermann-von-Helmholtz-Platz 1, D-76344 Eggenstein-Leopoldshafen, Germany
[3] Department of Mathematics, University of Utah, Salt Lake City, Utah 84112, USA
[4] Institute of Nanotechnology, Karlsruhe Institute of Technology (KIT), Hermann-von-Helmholtz-Platz 1, D-76344 Eggenstein-Leopoldshafen, Germany
E-mail: Tiemo.Bueckmann@kit.edu

Received 4 October 2013, revised 29 January 2014
Accepted for publication 3 March 2014
Published 26 March 2014

*New Journal of Physics* **16** (2014) 033032

doi:10.1088/1367-2630/16/3/033032

## Abstract

Dilational materials are stable, three-dimensional isotropic auxetics with an ultimate Poisson's ratio of –1. Inspired by previous theoretical work, we design a feasible blueprint for an artificial material, a metamaterial, which approaches the ideal of a dilational material. The main novelty of our work is that we also fabricate and characterize corresponding metamaterial samples. To reveal all modes in the design, we calculate the phonon band structures. On this basis, using cubic symmetry we can unambiguously retrieve all different non-zero elements of the rank-four effective metamaterial elasticity tensor from which all effective elastic metamaterial properties follow. While the elastic properties and the phase velocity remain anisotropic, the effective Poisson's ratio indeed becomes isotropic and approaches –1 in the limit of small internal connections. This finding is also supported by independent, static continuum-mechanics calculations. In static experiments on macroscopic polymer structures fabricated by three-dimensional printing, we measure Poisson's ratios as low as −0.8 in good agreement with the theory. Microscopic samples are also presented.

Keywords: mechanical metamaterials, acoustics, auxetics, dilational metamaterials

## 1. Introduction

Auxetic materials are rather special and unusual elastic solids. Their Poisson's ratio $\nu$ is negative, which means that it is easy to change their volume while fixing their shape, but it is hard to change their shape while fixing their volume [1]. This behavior is opposite to that of an ideal liquid [2] and to that of an ideal pentamode metamaterial [3]. In general, auxetic materials can be anisotropic, in which case the Poisson's ratio turns into a Poisson's matrix [4, 5]. There are no fundamental bounds for the values of the elements of the general Poisson's matrix [6]. In sharp contrast, there are established bounds for stable elastic isotropic media. Here, the Poisson's ratio [5] is connected to the ratio of bulk modulus $B$ (the inverse of the compressibility) and shear modulus $G$ via

$$\frac{B}{G} = \frac{1}{3}\frac{\nu + 1}{0.5 - \nu}. \tag{1}$$

For a stable elastic solid, neither the bulk nor shear modulus can be negative. For example, exerting a hydrostatic pressure onto a material with $B < 0$ would lead to an expansion, further increasing the pressure, the volume, etc. This non-negativity together with equation (1) immediately translates into the well-known interval of possible Poisson's ratios of $\nu \in [-1, 0.5]$. Effectively, isotropic auxetic materials with $\nu < 0$ composed of disordered polymer- or metal-based foams have been extensively studied in the literature; for a recent review see [7]. It is not clear though how one would systematically approach, along these lines, the ultimate limit of $\nu = -1$. Such ultimate extreme auxetic materials are called 'dilational' because they strictly support no other modes than dilations. Intuitively, for example, if one exerts a force onto a Statue of Liberty made of a dilational material at any point and along any direction, one can change its volume, but it will always maintain the exact shape of the Statue of Liberty. Obviously, this behavior is very different from that of a regular elastic solid. As an impact would be distributed throughout the entire elastic structure, dilational materials can, for example, be used as shock absorbers [8, 9]. Early three-dimensional auxetic metamaterials with anisotropic Poisson's ratios have recently been presented [10]. It is again not clear though how this approach [10] could be brought towards an isotropic behavior with $\nu = -1$. In the literature, several conceptual models for dilational metamaterials have been discussed [11–16]. These, however, contain elements like 'perfect joints' and 'rigid rods' that still need to be translated to a three-dimensional continuous microstructure composed of one constituent material (and vacuum in the voids) that can be fabricated using current technology. In this paper, inspired by the two-dimensional conceptual model of [11], we design a three-dimensional feasible blueprint for such a dilational material. On the basis of this blueprint, we also fabricate and characterize experimentally corresponding crystalline samples. The experiments form the main novelty of the present work. Several questions arise in the design process. Does this microstructure support unwanted easy modes other than the wanted dilations? Can this microstructure be described by a simple elasticity tensor and a constant mass density? For so-called Cosserat materials or for materials with anisotropic mass-density tensors [17–20], the answer would generally be negative. Our blueprint contains small internal connections mimicking the mentioned 'ideal joints'. How small do these connections have to be? The blueprint uses a simple-cubic translational lattice. Do we really get an isotropic Poisson's ratio? In general cubic elastic solids, the answer would be negative. To address all of these questions, we start by presenting the calculated phonon band structures for our blueprint. Next, we compare these with the static

continuum-mechanics calculations. These can then be directly compared with our static experiments on macroscopic polymer-based metamaterials made by three-dimensional printing. Finally, we show that microscopic versions can also be fabricated by recent advances in galvo-scanner dip-in direct-laser-writing (DLW) optical lithography. A related but different idea has recently been demonstrated by a rubbery chartreuse ball with 24 carefully spaced round dimples [21]. These buckliballs can also be arranged into bucklicrystals [22].

## 2. The blueprint

Our three-dimensional blueprint depicted in figure 1 is based on a recently published two-dimensional conceptual model [11]. This model contains 'ideal joints' and 'rigid bars'. In our blueprint, the ideal joints are implemented by small connections between the square and the triangular elements. Upon compression along one direction, for example from the top to the bottom, the inner squares rotate and the triangular outer connection elements get pulled inwards. Thus, ideally, the structure contracts laterally by the same amount as it contracts vertically. The Poisson's ratio would thus be $\nu = -1$. We will have to investigate to what extent we approach this ideal for a finite connection size $d$ compared to the cubic lattice constant $a$. Furthermore, the very thin rigid bars in [11] have been eliminated in our blueprint because they cannot be implemented using a single constituent material. As a result, it is not clear whether unwanted easy modes of deformation might occur. Indeed, in preliminary simulations, we have found that when using only one sense of rotation of the squares, the squares do not only rotate around their center, but also translate. To eliminate this unwanted easy mode, we use a three-dimensional checkerboard arrangement with the discussed motif alternating with its mirror image. The small cubes with a side length identical to the thickness of all squares and triangles are not necessary for the metamaterial function. They are, however, crucial as markers in our measurements of the Poisson's ratio (see below). They are hence considered in all our band structure and static calculations to allow for direct comparison.

## 3. Phonon band structures

The phonon band structure reveals all the modes of the elastic metamaterial, possibly including unwanted easy modes other than dilations (see above). The long-wavelength limit of the band structure can be the starting point for a description in terms of effective elastic metamaterial parameters (see next section). In our numerical band-structure calculations for the dilational metamaterial structure in figure 1, we solve the usual elastodynamic equations [23] for the displacement vector $\vec{u}(\vec{r}, t)$ containing the time-independent rank-four elasticity tensor $\overleftrightarrow{C}(\vec{r})$ and the scalar mass density $\rho(\vec{r})$, i.e.

$$\vec{\nabla} \cdot (\overleftrightarrow{C}\vec{\nabla}\vec{u}) - \rho\frac{\partial^2\vec{u}}{\partial t^2} = 0, \tag{2}$$

using a commercial software package (COMSOL Multiphysics, MUMPS solver). We impose Bloch-periodic boundary conditions onto the primitive cubic real-space cell shown in figure 1. We have carefully checked that all the results presented in this paper are converged. Typically, convergence is achieved using several tens of thousands of tetrahedra in one primitive real-space cell. We choose an isotropic polymer as the constituent material with Young's modulus

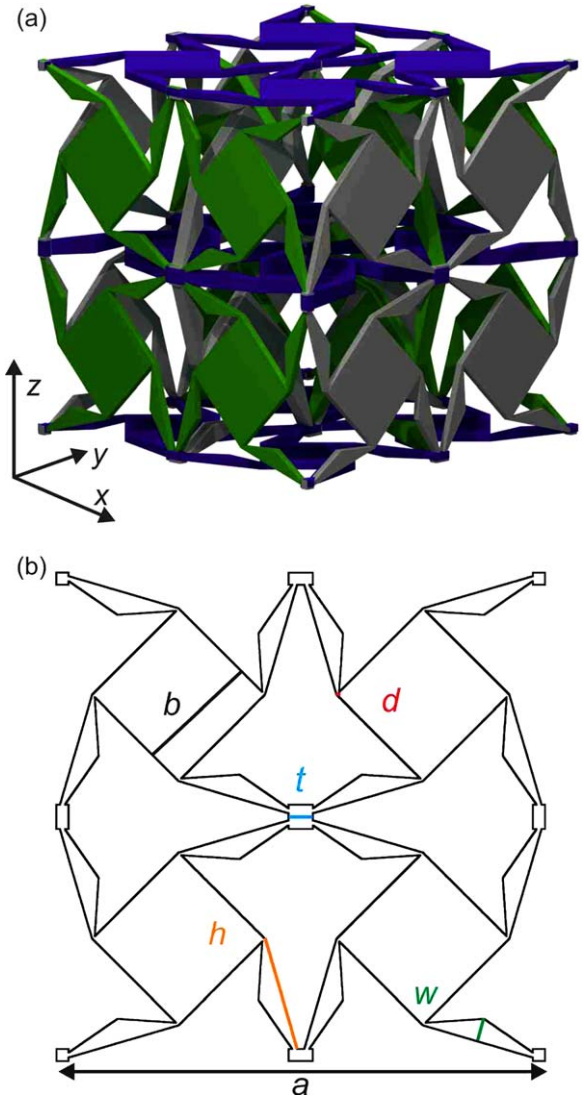


**Figure 1.** (a) Blueprint of a three-dimensional dilational metamaterial. A single unit cell is shown. This cell is composed of a checkerboard arrangement of a motif made of squares and triangles, and its mirror image. Everything is made from one material, however, different parts of the unit cell are colored for clarity. Faces of equal color (three for each color) are identical in shape when viewed from the same direction. They are only shifted along the normal face. As we display one unit cell, the faces at the surface of the unit cell are half as thick as the interior faces. (b) One plane of the structure, with geometrical parameters indicated. The cubic lattice constant is $a$. The other parameters are: block size $b/a = 0.25$, width of the holding element $w/a = 0.048$, layer thickness $t/a = 0.05$, holder length $h/a = 0.235$, and connection size $d/a = 0.5\%$.

1 GPa, Poisson's ratio 0.4, and mass density 1200 kg $m^{-3}$. These values are chosen according to the below experiments. Due to the scalability of the elastodynamic equations, our results can easily be scaled to isotropic constituent materials with any different Young's modulus and density. The Poisson ratio of the constituent material influences the results only to a very minor degree. The voids in the polymer are assumed to be vacuum. The lattice constant is chosen as

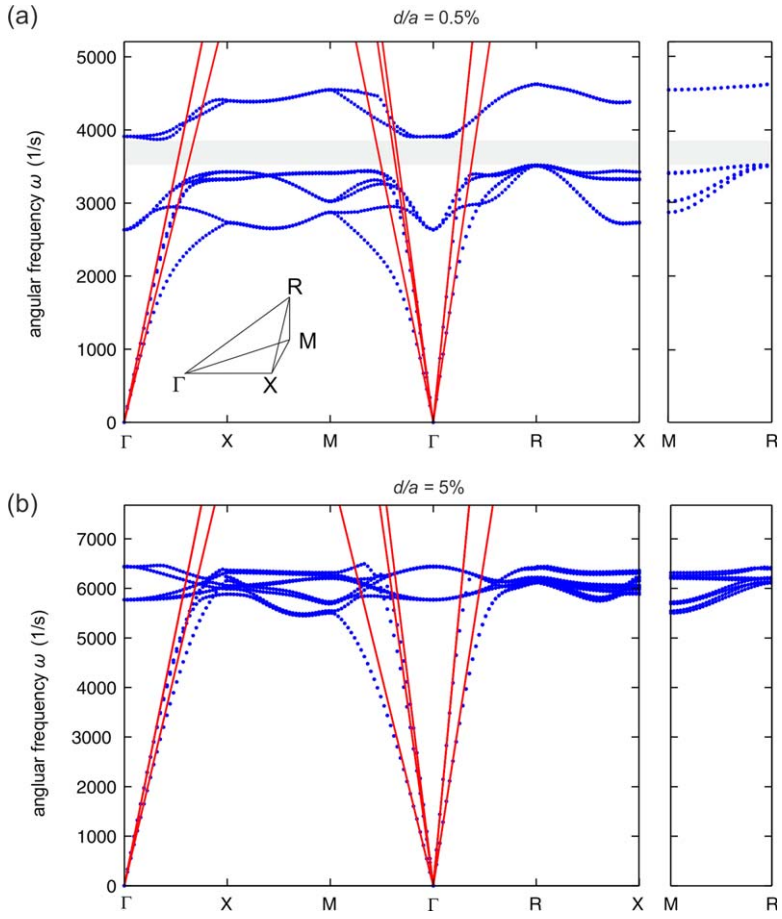


**Figure 2.** Calculated phonon band structures (blue dots) of dilational metamaterials, i.e. angular frequency $\omega$ versus wave vector for a tour along the high-symmetry points of the simple-cubic Brillouin zone (see inset in (a)). The straight red lines correspond to the effective-medium description of a cubic-symmetry crystal. (a) connection size $d/a = 0.5\%$, (b) $d/a = 5\%$; $a = 4.8$ cm. The gray area in (a) highlights a complete three-dimensional elastic band gap.

$a = 4.8$ cm according to our below experiments on macroscopic polymer structures. However, the results can again easily be scaled to any other value of $a$.

The crystal illustrated by figure 1 has inversion symmetry, three mirror planes normal to the principal cubic axes, and two-fold rotational symmetry along the same three axes. This two-fold rather than four-fold rotational symmetry means that the crystal does not have the same symmetry as the underlying simple-cubic translational lattice. It is rather an element of the point group $D_{2h}$ (in Schoenflies notation). However, our numerical calculations show that the band structure exhibits full cubic symmetry for the eight lowest bands, i.e. the eigenfrequencies for wave vectors along the $x$-, $y$-, $z$-directions are identical (not depicted). We thus represent the band structure results in a simple-cubic Brillouin zone. Examples of calculated band structures are depicted in figure 2 for two different values of the ratio $d/a$. Shown are the six lowest eigenmodes. It becomes immediately clear that the slope of the low-frequency or long-wavelength acoustic modes is not the same for all directions, it is anisotropic. Along the $\Gamma X$-direction (i.e. along the principal cubic axes), the velocity of the longitudinally polarized

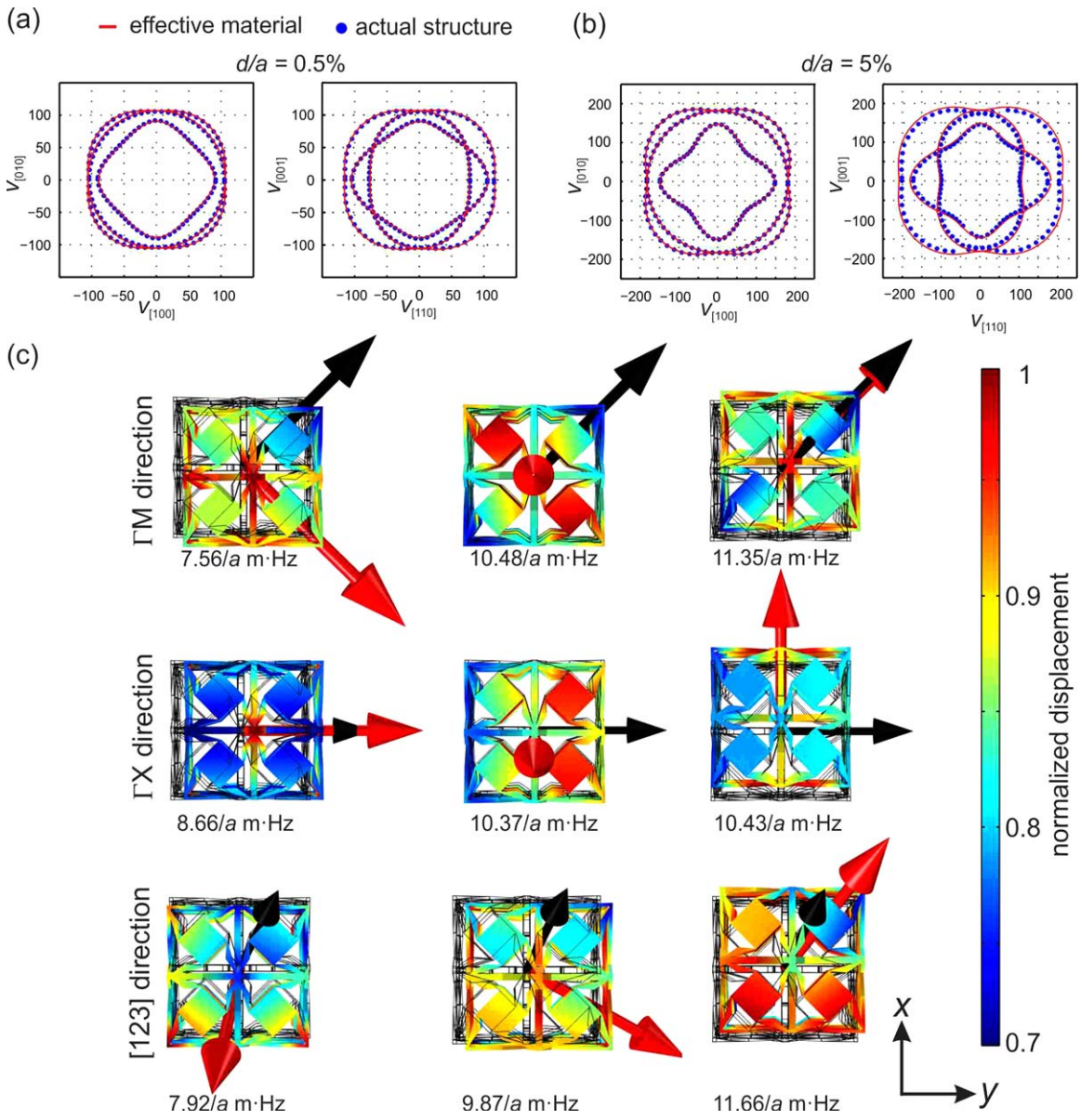


**Figure 3.** (a), (b) Polar representations of the phase velocity at a wave number of $k = 0.01/a$, i.e. the phase velocity in a particular direction is given by the radial length. The cut on the left is for the *xy*-plane, and the cut on the right for a plane spanned by the [111] and [110] directions. The cut on the left shows the four-fold rotational symmetry expected for a cubic structure. The connection size is (a) $d/a = 0.5\%$ and (b) $d/a = 5\%$. All other geometrical parameters are as quoted in figure 1. The blue dots are derived from the phonon band structure, and the red curves are the result of an effective-parameter description of a cubic-symmetry medium. (c) Selected eigenmodes for a fixed wave number of $k = 0.2/a$ and for $d/a = 0.5\%$. The corresponding eigenfrequencies scale proportionally to the inverse of the lattice constant $a$ (in units of m) and are quoted below each panel. They increase from left to right. The black arrows indicate the direction of the wave vector $\vec{k}$, and the red arrows the directions of the displacement

**Figure 3.** (Continued.) vector $\vec{u}$ averaged over one unit cell. Shown are the $\Gamma X$ direction identical to the principal cubic axes, and the $\Gamma M$ direction parallel to the cubic face diagonals, as well as for an oblique direction. For the latter, the modes are no longer purely transversely or longitudinally polarized. The normalized modulus of the local displacement vector $\vec{u}$ is shown by the false-color scale given on the right-hand side for the surface of the unit cell.

mode is smaller than that of the transversely polarized modes (see figure 3). In isotropic elastic media, the opposite holds true. As to be expected, the phase velocities are larger for larger $d/a$. We note in passing that the band structure in figure 2 for $d/a = 0.5\%$ exhibits a complete three-dimensional elastic (i.e. not only acoustic) band gap between normalized frequencies of 3.52 and 3.87 kHz. This region with a zero bulk phonon density of states corresponds to a gap-to-midgap ratio of 9%. This complements the other possibilities reported in the literature [23, 24]. To further emphasize the anisotropy, we also plot the phase velocity in polar diagrams in figure 3. Constant phase velocity would lead to circles in the two-dimensional cuts depicted. Clearly, the curves shown in figures 3(a) and (b) are not circular at all, neither for the small nor the large value of $d/a$. They do show four-fold symmetry though. This statement is not trivial, because the three orthogonal axes are not strictly equivalent in terms of the geometrical structure. This can be seen when comparing a view on the unit cell shown in figure 1 onto the *xy*- and the *xz*-planes. Nevertheless, the band structures show that wave propagation is equivalent for the three cubic axes.

The anisotropic behavior of the phase velocity is connected to rather complex underlying eigenmodes that are illustrated by the examples shown in figure 3(c). The red arrows point in the direction of the displacement eigenvector, averaged over all points in the unit cell. The black arrows are the corresponding wave vectors (their modulus is $0.2/a$). For waves propagating along the principal cubic axes or along the face diagonals, we find pure longitudinal or pure transverse polarization. For arbitrary oblique propagation directions with respect to the principal cubic axes, the eigenmodes are complicated mixtures of transverse and longitudinal polarization. In contrast, in an ideal isotropic elastic medium, the polarizations would be purely transverse or longitudinal.

## 4. Retrieval of the elasticity tensor

The phonon band structures presented in the previous section have shown pronounced anisotropies resulting from the cubic symmetry of the underlying translational lattice. In general, this also leads to an anisotropic Poisson's ratio $\nu$ [31]. In the limit of $\nu \to -1$ for compression along the principal cubic axes, one does, however, expect an isotropic behavior. To quantitatively investigate this important aspect of isotropy as a function of $d/a$, we derive a Poisson's ratio from the phonon band structure. To do so, we compare the band structures with the expectation from the continuum mechanics of an effective cubic-symmetry medium. For crystals obeying simple-cubic symmetry [25, 26], the rank-four elasticity tensor $\overleftrightarrow{C}$ has the three different non-zero elements $C_{11} = C_{22} = C_{33} = C_{1111} = C_{2222} = C_{3333}$, $C_{12} = C_{13} = C_{23} = C_{1122} = C_{2211} = C_{1133} = C_{3311} = C_{2233} = C_{3322}$, and $C_{44} = C_{55} = C_{66} = C_{2323} = C_{3232} = C_{2332} = C_{3223} = C_{1313} = C_{3131} = C_{1331} = C_{3113} = C_{1212} = C_{2121} = C_{1221} = C_{2112}$. Here, the elements with only two indices refer to the Voigt notation [27]. All other elements are zero. Furthermore, we

assume a constant scalar effective metamaterial mass density $\rho$, which is simply given by the volume filling fraction $f$ of the constituent material times its own bulk mass density (see figure 1). For $d/a = 0.5\%$ ($d/a = 5\%$), we get $f = 10.4\%$ ($f = 11.2\%$). On this basis, we can now calculate the phonon band structure in the long-wavelength limit. To do so, one needs to connect the phase velocities with the elements of $\overleftrightarrow{C}$ and with $\rho$. Here, it is convenient to inspect the $\Gamma M$ or [110] direction with three different phase velocities $v$ and three orthogonal eigenmodes that are either purely longitudinally (L) or purely transversely (T) polarized (see above). The latter either lie in the $xy$-plane or along the $z$-direction. Following [28], the connections are given by

$$C_{44} = \rho\,(v_{110}^{\mathrm{T},z})^2, \tag{3}$$

$$C_{12} = \rho\,(v_{110}^{\mathrm{L}})^2 - C_{44} - \rho\,(v_{110}^{\mathrm{T},xy})^2, \tag{4}$$

$$C_{11} = 2\,\rho\,(v_{110}^{\mathrm{T},xy})^2 + C_{12}. \tag{5}$$

The three different elements of $\overleftrightarrow{C}$ can immediately be computed from the three different phase velocities. One has to make sure though that the polarizations of the corresponding eigenmodes are the same as for the numerical band structure calculations. We have checked this aspect (not depicted). Furthermore, one needs to make sure that the elastic behavior is described for all other propagation directions as well. To this end, we compare in figures 2 and 3 the results from the phonon band structure (blue dots) with those of the effective-medium description (red lines). Obviously, we obtain excellent overall agreement for all conditions in the long-wavelength limit. This means that a description of the elastic metamaterial in terms of an elasticity tensor $\overleftrightarrow{C}$ for a cubic-symmetry effective medium is adequate. Having derived all non-zero elements of the effective metamaterial elasticity tensor, we can now apply established analysis to extract the Young's modulus $E$, the shear modulus $G$, the bulk modulus $B$ [29, 30], and the Poisson's ratio (or Poisson's matrix) [31]. We have

$$E = \frac{C_{11}^2 + C_{12}C_{11} - 2C_{12}^2}{C_{11} + C_{12}}, \tag{6}$$

$$G = C_{44}, \tag{7}$$

$$B = \frac{C_{11} + 2C_{12}}{3}. \tag{8}$$

Examples are given in table 1.

The Poisson's ratio for compression along the principal cubic axes is given by [29, 30]

$$\nu = \frac{C_{12}}{C_{11} + C_{12}}. \tag{9}$$

However, the Poisson's ratio might still be different for arbitrary oblique compression directions. Here, we use the more general expressions as given in [31], which are based on averaging along the directions normal to the compression direction.

$$\nu(\phi, \theta) = -\frac{\mathcal{A}r_{12} + \mathcal{B}(r_{44} - 2)}{16[C + \mathcal{D}(2r_{12} + r_{44})]}. \tag{10}$$

**Table 1.** Examples of retrieved effective parameters. The three non-equivalent non-zero elements of the elasticity tensor $C_{11}$, $C_{12}$, $C_{44} = G$, the Young's modulus $E$, and the bulk modulus $B$ are given for selected values of $d/a$.

| $d/a$ (%) | $C_{11}$ (MPa) | $C_{12}$ (MPa) | $C_{44} = G$ (MPa) | $E$ (MPa) | $B$ (MPa) |
|---|---|---|---|---|---|
| 5 | 2.7 | 0.0051 | 4.0 | 2.7 | 0.89 |
| 4 | 2.4 | −0.16 | 3.8 | 2.4 | 0.69 |
| 3 | 2.0 | −0.35 | 3.4 | 1.9 | 0.43 |
| 1.25 | 1.3 | −0.52 | 2.1 | 0.61 | 0.086 |
| 0.75 | 1.1 | −0.51 | 1.7 | 0.33 | 0.042 |
| 0.5 | 1.0 | −0.46 | 1.4 | 0.20 | 0.025 |
| 0.25 | 0.85 | −0.41 | 1.1 | 0.12 | 0.014 |

Introducing the compliance tensor $\overleftrightarrow{S} = \overleftrightarrow{C}^{-1}$, the abbreviations in (10) are given by

$$r_{12} = \frac{S_{12}}{S_{11}},$$

$$r_{44} = \frac{S_{44}}{S_{11}},$$

$$\mathcal{A} = 2\left[53 + 4\cos(2\theta) + 7\cos(4\theta) + 8\cos(4\phi)\sin^4(\theta)\right],$$

$$\mathcal{B} = -11 + 4\cos(2\theta) + 7\cos(4\theta) + 8\cos(4\phi)\sin^4(\theta),$$

$$\mathcal{C} = 8\cos^4(\theta) + 6\sin^4(\theta) + 2\cos(4\phi)\sin^4(\theta),$$

$$\mathcal{D} = 2\left[\sin^2(2\theta) + \sin^4(\theta)\sin^2(2\phi)\right].$$

Here, as usual, $\phi$ and $\theta$ are the azimuthal and polar angle, respectively, in spherical coordinates. The resulting direction dependence of the Poisson's ratio is visualized in two different ways in figures 4 and 5. Figure 4 is the generalized polar representation, i.e. the Poisson's ratio is proportional to the length of the vector from the origin to the depicted surface. The Poisson's ratio is also visualized by the false-color scale. For large connections, e.g. for $d/a = 5\%$, the behavior is obviously far from isotropic. Furthermore, the effective metamaterial Poisson's ratio is far from –1. For a decreasing connection size $d/a$, the effective metamaterial Poisson's ratio $\nu$ becomes more negative and reaches an almost isotropic behavior at $d/a = 0.25\%$. This means that experiments need to realize values of $d/a$ below 1% or better. Figure 5 depicts the derived minimum and maximum values of $\nu$ versus $d/a$. For the smallest numerically accessible values of $d/a$, the Poisson's ratio comes close to –1. The data do not appear to extrapolate to exactly –1 though. We suspect that this aspect is due to the small cubes in our blueprint that we have introduced for experimental reasons (see above). We expect that the effective metamaterial Poisson's ratio would converge to –1 in the hypothetical limit of no cubes and $d/a \to 0$, which cannot be realized experimentally though.

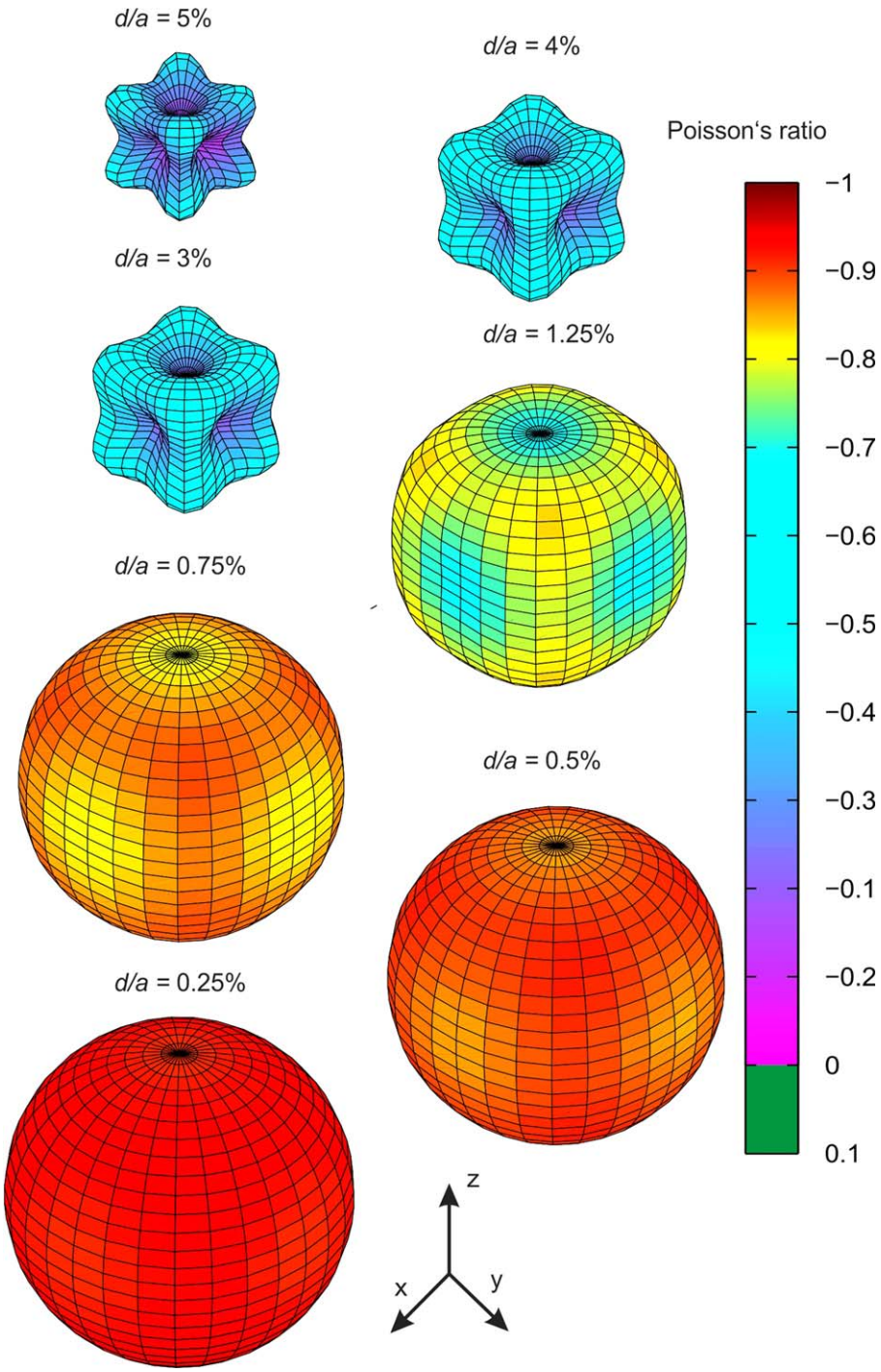


**Figure 4.** Three-dimensional polar diagram of the effective metamaterial Poisson's ratio $\nu$, i.e. the length of the vector from the origin to the surface is proportional to the modulus of the Poisson's ratio. The Poisson's ratio including its sign is also indicated by the false-color scale. As the $d/a$ ratio decreases, $\nu$ becomes more negative and more isotropic, eventually approaching the ultimate limit of −1 for an isotropic elastic material. These results are derived from the band structures as exemplified in figure 2 and for the other geometrical parameters as in figure 1.

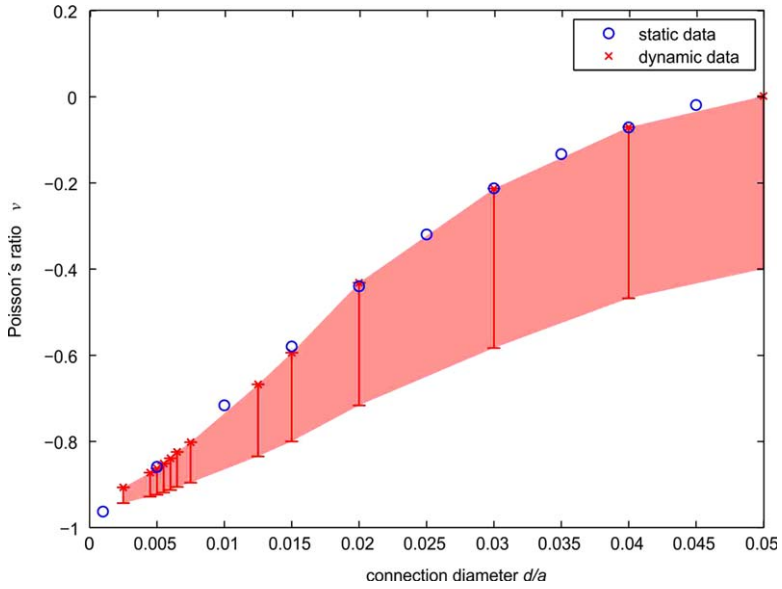


**Figure 5.** The minimum and maximum effective metamaterial Poisson's ratio (see figure 4) versus $d/a$ ratio. The red symbols are the minima and maxima derived from the phonon band structures, and the blue dots are obtained from static continuum-mechanics calculations for compression along one of the principal cubic axes.

## 5. Static continuum-mechanics calculations

Often, the Poisson's ratio is measured in (quasi-)static experiments. To derive the Poisson's ratio, one compresses along one direction, e.g. the $z$-direction, leading to a certain strain (or relative displacement) $\varepsilon_{zz}$, observes or calculates the displacement along the orthogonal $x$-direction (or the orthogonal $y$-direction), hence the element of the strain tensor $\varepsilon_{xx}$, and computes the Poisson's ratio according to its definition

$$\nu = -\frac{\varepsilon_{xx}}{\varepsilon_{zz}}. \tag{11}$$

Furthermore, experiments are based on finite-size samples also containing a finite number of unit cells only. For metamaterials, the number of unit cells may be rather small. We thus also investigate the question to what extent are measurement artifacts expected for accessible-sized samples. The numerical calculations to be presented in this section have been performed with COMSOL Multiphysics using the Structural Mechanics Module. The geometry of the structure is created using the CAD COMSOL Kernel. The mesh is created within COMSOL Multiphysics using the preset parameter values called 'normal' meshing with settings: maximum element size = $0.1a$, minimum element size = $0.018a$, maximum element growth rate = 1.5, resolution of curvature = 0.6, resolution of narrow regions = 0.5. For example, for a connection size of $d/a = 0.5\%$, this leads to about 90 000 tetrahedral elements. We use the MUMPS Solver. In convergence tests, we have verified that the derived effective metamaterial Poisson's ratios are accurate to within 0.01. All geometrical parameters and constituent material parameters are as given above. To mimic a fictitious infinitely extended crystal, we assume that all unit cells behave the same way (analogous to the zero wave vector in the previous section or to the Taylor (Voigt) assumption in [32, 33]). For convenience, we choose our frame of

reference such that the crystal center of mass is fixed. For compression along one principal cubic axis, these conditions can be implemented by imposing anti-symmetric boundary conditions (corresponding to periodic conditions allowing for a volume change) onto a single cubic unit cell. This means that the normal component of the displacement vector on the surface of the unit cell is constant on this surface and equal to the negative of the normal component on the opposing surface. To investigate the linear regime, we choose strains along the compression direction of 1%. The resulting behavior is illustrated in figure 6(a). The length of the (black) arrows is exaggerated and indicates the local displacement vectors. The false-color scale shows the modulus of the local displacement vector. Note that the corners of the unit cell move almost diagonally towards the center. The Poisson's ratio can immediately be computed from the components of these displacement vectors. For example, for $d/a = 0.75\%$ corresponding to our below experiments, we obtain $\nu = -0.79$. We note in passing that the other points within the unit cell generally move in different directions than the corners. This has important implications for our below experiments in that we must not evaluate the movement of all points within the unit cell, but rather only of the corners (which are representative of the macroscopic deformation). To have a finite region for imaging and tracking, we have introduced the small cubes in figure 1. The results of $\nu$ versus $d/a$ are shown in blue in figure 5. Obviously, the agreement of these (static) values with those derived from the (dynamic) phonon band structures is good, giving further validity to our results. The most negative dynamic results tend to be more negative than the static ones. For example, for $d/a = 0.75\%$, the minimum dynamic value is $\nu = -0.895$, the static one $\nu = -0.79$. Static calculations have also been performed for a finite metamaterial sample containing $2 \times 2 \times 2$ unit cells (see figure 1) as shown in figure 6(b), to directly compare these with the experiments. Here, we assume sliding boundary conditions in the plane normal to the compression direction. Good agreement together with the calculations for the infinite crystals as above will allow us to extract Poisson's ratios under these conditions. Figure 6(b) is an example for a finite crystal composed of $2 \times 2 \times 2$ unit cells. To compare with the experiments to be discussed below, one can measure the lateral strain of the left and right outer corners in the middle of the horizontal direction (see small circles) and divide these by the relative axial shift of the stamps. We obtain a Poisson's ratio for the finite crystal of $-0.76$, which is not too far from the one for the fictitious infinitely extended crystal of $\nu = -0.79$ in panel (a) of the same figure. These parameters have been chosen to match those of the experiments to be discussed next.

## 6. Macroscopic dilational metamaterials

We fabricated macroscopic (this section) and microscopic (next section) versions of the blueprint shown in figure 1. The macroscopic samples were fabricated with the Objet30 printer sold by Objet (now Stratasys), USA. For the metamaterial, we used the basic polymer ink 'FullCure850 VeroGray'. During the fabrication, however, one also needs a support material. The default is a mixture of 'FullCure850 VeroGray' and 'FullCure705 Support' that we were not able to remove from the composite. Thus, we exclusively chose 'FullCure705 Support', which can be etched out in a bath of NaOH base after hand cleaning. The structure files are exported in STL file format directly from the geometry used in the COMSOL Multiphysics calculations and are imported into the Objet printer. The printing is done automatically using a standard process. An example of a fabricated macroscopic metamaterial structure is shown in

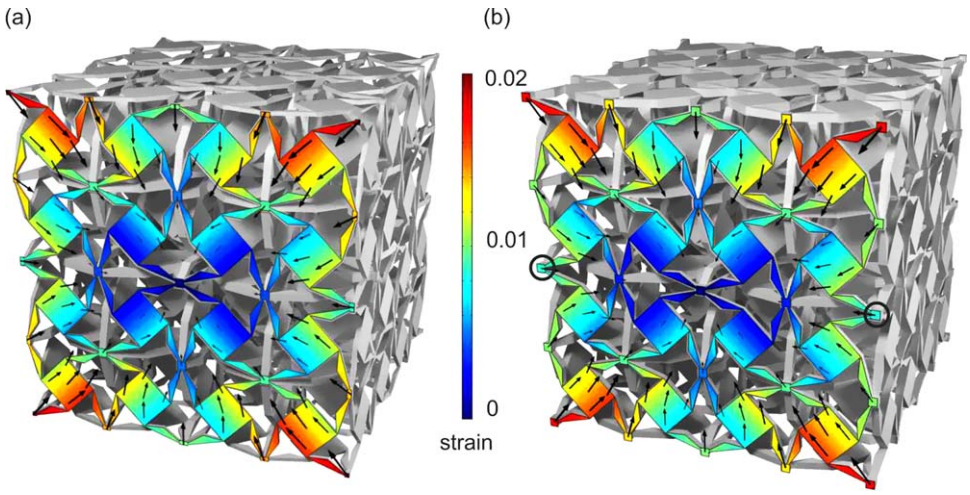


**Figure 6.** (a) $2 \times 2 \times 2$ unit cells (compare figure 1) out of an infinite crystal compressed along the $z$-direction. The resulting in-plane strain for an axial strain of 0.01 is depicted by the false-color scale projected onto the front surface of the cube as well as by the black arrows. (b) The same, but for a finite crystal with $2 \times 2 \times 2$ unit cells.

figure 7(a). The geometrical parameters are as defined in figure 1 with $d/a = 0.75\%$ and $a = 4.8$ cm. According to previous measurements [34], the constituent polymer has a Young's modulus in the range of $E = 0.7$–$2$ GPa. The measurement setup for the macroscopic samples consists of two metallic stamps and a linear stage containing a force cell. The sliding boundary conditions (see previous section) are achieved by placing the watered sample between the stamps. We attempted to implement fixed boundary conditions by gluing the sample to the stamp using double-sided tape. This led to the same lateral displacements of the sample, indicating very strong forces parallel to the stamps, which suggests that assuming sliding boundary conditions is adequate. We gradually compressed the sample by moving one stamp with a linear stage while fixing the other stamp, and recorded the images of one of the sample surfaces. These images were taken with a Canon EOS 550D camera in full HD ($1920 \times 1080$ pixels) resolution and at 24 frames per second. The objective lens (Tamron SP 70–300 mm f/4-5,6 Di VC USD) is located at a distance of approximately 1.5 m to the sample. We checked that the image distortions (e.g. barrel-type aberrations) were sufficiently small to not influence our experiments. The displacements of the corners of the unit cells were tracked using an autocorrelation approach used previously [10]. Multiple measurements with increasing maximum strain for a crystal composed of $2 \times 2 \times 2$ unit cells (see figure 7(a)) are depicted in figure 7(b). The graph shows the strain along the horizontal direction ($x$) versus the strain along the axial compression direction ($z$). The solid red curve corresponds to two measurement cycles, i.e. the sample is compressed, released and compressed and released again. Clearly, the four parts are hardly distinguishable, indicating an almost reversible elastic behavior. From fits with straight lines (see green dots) we deduce a Poisson's ratio of $-0.76 \pm 0.02$. The corresponding numerically calculated strains for a finite sample with $2 \times 2 \times 2$ unit cells are shown as black dots. Using the identical structure parameters but assuming an infinite crystal (see previous section), we get a Poisson's ratio of $\nu = -0.79$. We note in passing that we have simultaneously measured the axial force from a load cell (not depicted). For $d/a = 0.75\%$, we obtain a metamaterial Young's modulus of $E = 0.16$ MPa. For the same $d/a$ value, we obtained

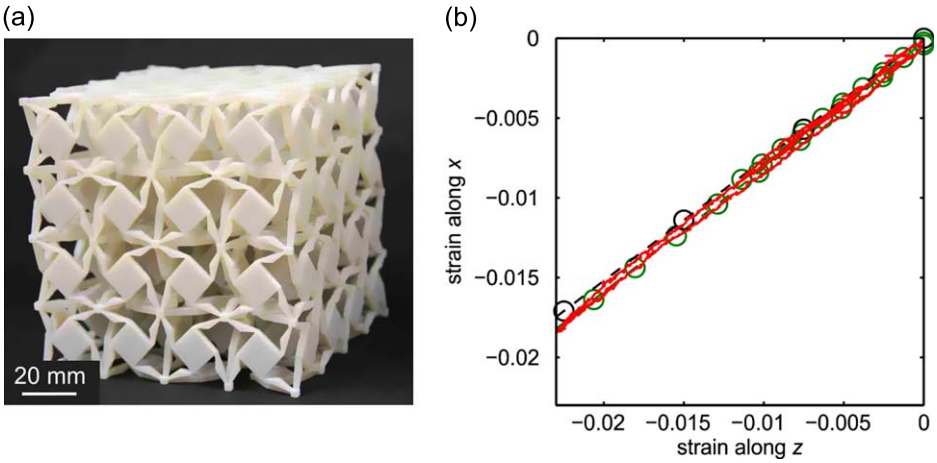


**Figure 7.** (a) Photograph of a macroscopic polymer-based finite crystal with $2 \times 2 \times 2$ unit cells fabricated by 3D printing, following the blueprint and the parameters given in figure 1(b). The measured lateral versus axial strain (solid red curve) is obtained from an image correlation approach upon compression along the vertical $z$-direction. The green circles on the straight lines correspond to a Poisson's ratio of $-0.76$ and $-0.77$, respectively, and the black circles to numerical calculations for $d/a = 0.75\%$. Extrapolation to an infinite three-dimensional crystal (see previous section) delivers a Poisson's ratio of $\nu = -0.79$.

$E = 0.33$ MPa from the theory (see table 1). Given the significant error in the constituent polymer Young's modulus quoted above, these values are roughly consistent.

## 7. Microscopic dilational metamaterials

The structures shown in the preceding section have validated our theoretical blueprint of a three-dimensional dilational metamaterial, but they hardly qualify as a 'material' in the normal sense. Thus, it is interesting to ask whether corresponding structures with lattice constants $a$ that are two to three orders of magnitude smaller are in reach. Also, it would be highly desirable to obtain structures containing a larger total number of unit cells. We have thus also fabricated microscopic structures based on the same blueprint (without the small blocks for tracking). To fabricate such microscopic dilational metamaterial samples, photoresist samples are prepared by drop-casting the commercially available negative-tone photoresist 'IP-Dip' (Nanoscribe GmbH, Germany) on diced silicon wafers ($22 \times 22$ mm). We used the commercial DLW system Photonic Professional GT (Nanoscribe GmbH, Germany). In this instrument, the liquid photoresist is polymerized via two-photon absorption using a 40 MHz frequency-doubled Erbium fiber laser with a pulse duration of 90 fs. To avoid depth-dependent aberrations, the objective lens (with numerical aperture NA = 1.3 or NA = 0.8, Carl Zeiss) is directly dipped into the resist. The laser focus is scanned using a set of pivoted galvo mirrors. Structural data are again created in STL file format using the open-source software Blender and COMSOL Multiphysics. Due to the demanding critical distances of the mechanical metamaterials, the scan raster is set to 200 nm (400 nm) laterally and 300 nm (800 nm) axially for the NA = 1.3 (NA = 0.8) objective lens. Each individual layer is scanned in the so-called skywriting mode, i.e. while the laser focus is scanned continuously, the laser power is switched between 0 mW

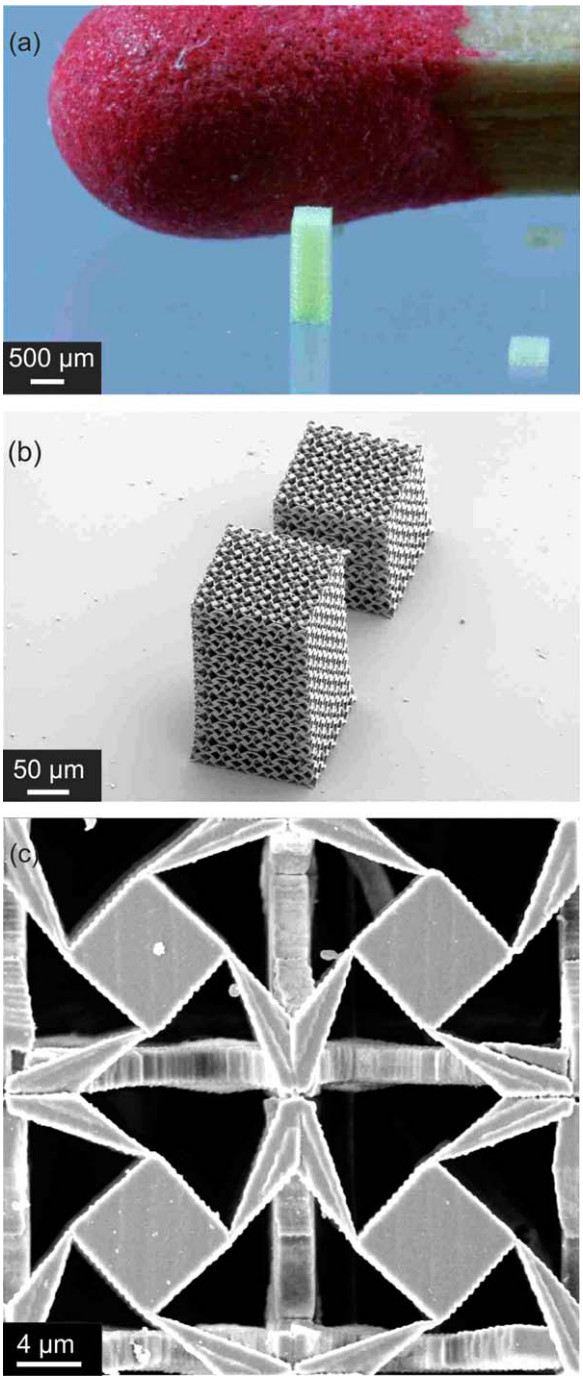


**Figure 8.** Gallery of polymer dilational metamaterial microstructures with different sizes and aspect ratios, following the blueprint illustrated in figure 1 (without the small cubic tracking markers), all fabricated by 3D dip-in direct laser writing. (a) Photograph of a structure with $3 \times 3 \times 9$ unit cells (and a smaller one on the right-hand side), $a = 180\,\mu$m. (b) Electron micrograph of two microstructure samples with overall aspect ratios of 1:1 and 2:1, respectively, $a = 35\,\mu$m. (c) Magnified view onto one unit cell of the structure, revealing details within the unit cell (compare figure 1), $a = 35\,\mu$m.

(no exposure) and about 13 mW or higher (exposure) to build up the fine features of the metamaterial. The writing speed is set to 20 mm $s^{-1}$. After DLW of the preprogrammed pattern, the exposed sample is developed for 20 min in isopropanol and acetone. The process is finished in a supercritical point dryer to avoid capillary forces during drying.

Optical and electron micrographs of different samples are depicted in figure 8. The sample in panel (a) has overall dimensions of $0.54 \times 0.54 \times 1.62$ mm ($3 \times 3 \times 9$ unit cells), yet, at the same time, minimum feature sizes in the sub-micron range. However, due to the smaller lattice constants, it is not possible to resolve the details within the unit cell to track the positions of the small marker cubes for measuring the Poisson's ratio, as performed for the macroscopic samples.

## 8. Conclusion

We have designed, fabricated and characterized a three-dimensional microstructure based on a simple-cubic translational lattice that effectively acts as an auxetic, converging for small internal connections $d/a \to 0$ to the ultimate limit of an isotropic three-dimensional dilational metamaterial of $\nu = -1$. Our experiments approach this limit. Interestingly, the Poisson's ratio becomes isotropic in the limit $d/a \to 0$, whereas the acoustic phase velocity and other elastic properties remain anisotropic. If fabricated in larger volumes and composed of different constituent materials, such dilational metamaterials might find applications in terms of shock absorbers. In our treatment, we have derived all the elements of the effective metamaterial elasticity tensor and hence all elastic parameters by comparing the phonon band structure in the long-wavelength limit with the continuum mechanics of the homogeneous media. This parameter retrieval could be of interest for other cubic-symmetry elastic metamaterials beyond the specific example discussed here.

## Acknowledgments

We would like to thank the DFG-Center for Functional Nanostructures (CFN), the Karlsruhe School of Optics & Photonics (KSOP), and the National Science Foundation through grant DMS-1211359 for their support. We acknowledge support by Deutsche Forschungsgemeinschaft and the Open Access Publishing Fund of Karlsruhe Institute of Technology.

## References

[1] Feynman R, Leighton R and Sands M 2011 *The Feynman Lectures on Physics* (New York: Basic Books)
[2] Born M 1939 Thermodynamics of crystals and melting *J. Chem. Phys.* **7** 591
[3] Kadic M, Bückmann T, Stenger N, Thiel M and Wegener M 2012 *Appl. Phys. Lett.* **100** 191901
[4] Li Y 1976 *Phys. Status Solidi* A **38** 171–5
[5] Rand O and Rovenski V 2004 *Analytical Methods in Anisotropic Elasticity: With Symbolic Computational Tools* (Basel: Birkhäuser)
[6] Ting T C T and Chen T 2005 *Q. J. Mech. Appl. Math.* **58** 73–82
[7] Greaves G N, Greer A L, Lakes R S and Rouxel T 2011 *Nat. Mater.* **10** 823–37
[8] Alderson A 1999 *Chem. Ind.* (London) **10** 384–91

[10] Bückmann T, Stenger N, Kadic M, Kaschke J, Frölich A, Kennerknecht T, Eberl C, Thiel M and Wegener M 2012 *Adv. Mater.* **24** 2710–4
[11] Milton G W 2013 *J. Mech. Phys. Solids* **61** 1543–60
[12] Milton G W 1992 *J. Mech. Phys. Solids* **40** 1105–37
[13] Lakes R and Wojciechowski K W 2008 *Phys. Status Solidi* B **245** 545–51
[14] Prall D and Lakes R S 1997 *Int. J. Mech. Sci.* **39** 305–14
[15] Mitschke H, Schwerdtfeger J, Schury F, Stingl M, Körner C, Singer R F, Robins V, Mecke K and Schröder-Turk G E 2011 *Adv. Mater.* **23** 2669–74
[16] Grima J N and Evans K E 2000 *J. Mater. Sci. Lett.* **19** 1563–5
[17] Cosserat E and Cosserat F 1909 *Théorie des corps déformables* (Paris: Hermann)
[18] Torrent D and Sanchez-Dehesa J 2008 *New J. Phys.* **10** 023004
[19] Milton G W, Briane M and Willis J R 2006 *New J. Phys.* **8** 248
[20] Schoenberg M and Sen P N 1983 *J. Acoust. Soc. Am.* **73** 61–67
[21] Krieger K 2012 *Nature* **448** 146–7
[22] Babaee S, Shim J, Weaver J C, Chen E R, Patel N and Bertoldi K 2013 *Adv. Mater.* **25** 5044–9
[23] Deymier P 2013 *Acoustic Metamaterials and Phononic Crystals* (Berlin: Springer)
[24] Wang Y F and Wang Y S 2013 *J. Vib. Acoust.* **135** 041009
[26] Kittel C 1995 *Introduction to Solid State Physics* vol 7 (New York: Wiley)
[27] Voigt W 1910 *Lehrbuch der Kristallphysik: mit Ausschlußd. Kristalloptik* (Leipzig: BSB Teubner)
[28] Tsang T and Park H Y 1983 *Phys. Lett.* **99A** 377–80
[29] Bowers A F 2009 *Applied Mechanics of Solids* (Boca Raton, FL: CRC)
[30] Hill R 1952 *Proc. Phys. Soc.* A **65** 349–54
[31] Wojciechowski K W 2005 *Comput. Methods Sci. Technol.* **11** 73–79
[32] Geers M G D, Kouznetsova V G and Brekelmans W A M 2008 *J. Comput. Appl. Math.* **234** 2175–82
[33] Kouznetsova V G 2002 *Computational homogenization for the multi-scale analysis of multi-phase materials* (Eindhoven: Technische Universiteit)
[34] Schittny R, Bückmann T, Kadic M and Wegener M 2013 *Appl. Phys. Lett.* **103** 231905